Journal of Structural Biology: X 7 (2023) 100081

Contents lists available at ScienceDirect

Journal of Structural Biology: X

journal homepage: www.sciencedirect.com/journal/journal-of-structural-biology-x

Temporal dynamics of charge buildup in cryo-electron microscopy

Makoto Tokoro Schreiber [a,1], Alan Maigné [a,2], Marco Beleggia [b,3], Satoshi Shibata [a,4], Matthias Wolf [a,c,*]

[a] Molecular Cryo-Electron Microscopy Unit, Okinawa Institute of Science and Technology Graduate University, 1919-1 Tancha, Onna-son, Okinawa, Japan
[b] DTU Nanolab, Technical University of Denmark, 2800 Kgs. Lyngby, Denmark
[c] Institute of Biological Chemistry, Academia Sinica, Nankang, Taipei 115, Taiwan

ARTICLE INFO

Edited by "Bauke W. Dijkstra"

Keywords:
Cryo-electron microscopy
Specimen charging
Ice
Defocused diffraction
Fresnel diffraction

ABSTRACT

It is well known that insulating samples can accumulate electric charges from exposure to an electron beam. How the accumulation of charge affects imaging parameters and sample stability in transmission electron microscopy is poorly understood. To quantify these effects, it is important to know how the charge is distributed within the sample and how it builds up over time. In the present study, we determine the spatial distribution and temporal dynamics of charge accumulation on vitreous ice samples with embedded proteins through a combination of modeling and Fresnel diffraction experiments. Our data reveal a rapid evolution of the charge state on ice upon initial exposure to the electron beam accompanied by charge gradients at the interfaces between ice and carbon films. We demonstrate that ice film movement and charge state variations occur upon electron beam exposure and are dose-rate dependent. Both affect the image defocus through a combination of sample height changes and lensing effects. Our results may be used as a guide to improve sample preparation, data collection, and data processing for imaging of dose-sensitive samples.

1. Introduction

The electrostatic charging of samples when imaged with an electron beam has been a long-standing problem for electron microscopy. Charging is typically due to the release and recapture of secondary electrons (SEs) rather than the embedding of primary electrons (Cazaux, 1993; Cazaux, 2004). The charge accumulation affects the surface potential of the sample and SE yield; leading to a complex temporal evolution. Charging is particularly noticeable in scanning electron microscopy (SEM) as the low energy of the primary electrons make them more sensitive to surface potentials. Therefore, charging behavior has been more extensively studied in SEM (Cazaux, 1993; Cazaux, 2004; Cazaux, 2006; Curtis and Ferrier, 1969; Renoud et al., 1998). In transmission electron microscopy (TEM), the effects of charging on samples and image formation can be more subtle and are poorly understood. In cryogenic electron microscopy (cryo-EM), where electron-radiation sensitive organic specimens embedded in vitreous ice are imaged with low electron doses and 3D structures are reconstructed from many images of identical particles, charging effects are thought to limit resolution. The advent of fast and sensitive direct electron detection cameras has enabled the practice of acquiring dose-fractionated image stacks ("movies") rather than static images integrated over equivalent doses. These stacks are post-processed with image alignment (Rubinstein and Brubaker, 2015; Zheng et al., 2017; Scheres, 2014) and dose weighting (Grant and Grigorieff, 2015) algorithms to extract more information than was achieved earlier by image integration. In dose weighting procedures, latter frames contribute primarily with lower resolution information as samples are progressively damaged throughout the serial acquisition. In principle, the first few frames should contribute with the highest-resolution information as the protein structure is near-pristine. In practice however, the first few frames are found to contribute little information to the final 3D reconstruction (Vinothkumar et al., 2016).

* Corresponding author at: Molecular Cryo-Electron Microscopy Unit, Okinawa Institute of Science and Technology Graduate University, 1919-1 Tancha, Onna-son, Okinawa, Japan.
E-mail address: matthias.wolf@oist.jp (M. Wolf).
[1] Present address: University of Alberta, Edmonton, Alberta T6G 2M9, Canada.
[2] Present address: ETH Zurich, ScopeM HPM D 44.2, 8093 Zurich, Switzerland.
[3] Present address: Universitá degli Studi di Modena e Reggio Emilia, 41125 Modena, Italy.
[4] Present address: Tottori University, Div. Bacteriology, Dept. Microbiology & Immunology, Faculty of Medicine, Tottori 683-8503, Japan.

https://doi.org/10.1016/j.yjsbx.2022.100081

Available online 30 December 2022

The cause of this information degradation is not fully understood, although it is suspected that beam-induced sample motion and charging effects might play a significant role.

Recently, Bayesian predictions of particle motion in the first few frames has succeeded in recovering additional information (Zivanov et al., 2019); demonstrating that rapid particle movement does indeed contribute to the image degradation. Solid evidence in the literature (Brink et al., 1998; Brink et al., 1998; Russo and Henderson, 2018; Cazaux, 1995) indicates that the insulating amorphous ice films accumulate positive charges due to the emission of secondary electrons that are not compensated by grounding currents. This accumulation of charges acts as a weak electrostatic lens – thereby altering imaging parameters such as defocus and other low-order aberrations.

While the qualitative behavior of the sample charging process is partially known, the spatial charge distribution and temporal charge evolution have not yet been quantified. In this work, we quantify the distribution and evolution of charges on ice films illuminated with beam conditions typical of those used in cryo-EM. This is achieved by fitting Fresnel diffraction data obtained at high-frame rates to simulated Fresnel diffraction patterns from different charge distributions. This work will aid in the understanding of how charging dynamics affect the imaging process in cryo-EM and what steps may be taken to avoid charging and recover more information from datasets. The principles understood from this study should also be applicable to the imaging of other thin insulating samples in TEM.

2. Methods

We acquired Fresnel diffraction images with a parallel electron beam passing through amorphous ice films as a function of exposure time (accumulated dose). As shown in Fig. S1, charge accumulation on the ice film establishes an electric field that has a lensing effect on subsequent electrons. The Fresnel diffraction pattern evolves accordingly. Previous works have investigated this phenomenon qualitatively as a function of beam position (Brink et al., 1998; Berriman and Rosenthal, 2012; Curtis and Ferrier, 1969). With the improved sensitivity and read-out speed of direct electron detection cameras, we are now in the position to investigate the temporal dynamics of the charging process directly upon exposing the sample to an electron beam. By combining the data with Fresnel diffraction simulations from charge distribution models, we quantify the temporal charging behavior of electron-irradiated thin films.

2.1. Experimental

Samples of vitreous ice with embedded proteins were prepared on Quantifoil holey carbon grids (Quantfoil Micro Tools, Germany) with 1.2μm diameter holes by standard plunge freezing methods in a Vitrobot (Thermo Fisher Scientific, TFS). The samples were loaded into a Titan Krios cryo-TEM (TFS) equipped with an energy filter (Gatan Quantum 968) and a K2 direct detection camera (3838 × 3710 array of 5μm pixels, Gatan). Nano probe illumination (50 μm C2 aperture) was used to produce a 913 nm diameter parallel beam which could illuminate the ice films within the quantifoil grid holes without exposing any adjacent carbon film (Fig. S2). Different sample holes (ice films) were measured with the same beam size, objective lens focus, and diffraction lens focus values. The beam conditions were set to electron dose-rates of 0.36, 0.48, 0.84, 1.51$e^-/Å^2/s$ (corresponding to "spot sizes" of 11, 10, 9, 8 on the microscope). Once the beam position and parameters were set, the projector lenses were set to view the diffraction plane with a camera length setting of 4.3 m on the post energy-filter camera (giving an effective camera length of 38.7m). The diffraction spot was then highly under focused so that the imaged plane is far from the charged and uncharged back focal planes (BFP) and the beam is well spread on the camera. The beam was blocked with the gun-blanker before exposing the sample for recording. The defocused zero-order spot was then recorded on the direct electron detector in unfiltered counting mode as a movie with a given frame rate and recording time using a custom Digital Micrograph script.

An example of a recorded movie is shown in Fig. 1 and supp. dat. 1. In the first frame, the electron beam enters the frame as the electrostatic pre-specimen shutter is released; causing the beam image to be blurred. From the second frame onwards, the beam is clearly visible and observed to shrink slightly in the first few frames before becoming roughly constant in size at higher accumulated electron dose. In the first few frames, Fresnel fringes are visible only near the beam edges, while in latter frames they extend to the center of the beam.

To connect the recorded Fresnel diffraction data to sample charge accumulation and quantify the charging dynamics we developed and applied models of realistic expected charge distributions on the illuminated films.

2.2. Charge distribution modeling

Lensing effects are caused by parabolic phase shift profiles. For electron waves, such phase profiles can be imparted by the electrostatic potential ensuing from a given charge distribution within a sample. For simplicity, we assume that the samples are two-dimensional such that the charging is completely surface bound. We hypothesize three possible charge distributions and calculate the resulting phase shift profiles on impinging electron plane-waves. From this, we simulate Fresnel diffraction patterns by wave propagation algorithms according to standard image formation theory.

Three axially symmetric surface charge density distributions were considered. Two of them contain a total charge Q within the illuminated beam area with radius R_b. The first is a uniform charge density represented by a top-hat function

$$\sigma_{\mathrm{uq}}(r) = \begin{cases} \dfrac{Q}{\pi R_b^2}, & r \leqslant R_b \\ 0, & r > R_b \end{cases} \tag{1}$$

where r is the polar radial coordinate originating at the center of the illuminated area. The second charge distribution is nearly equipotential at the surface of the sample (hereafter referred to as the "equipotential charge distribution" for brevity). It is obtained from the equilibrium charge distribution on a conducting disk (Ciftja, 2020). In one dimension, the equipotential surface charge distribution is equivalent to a uniform charge distribution. In two dimensions, as considered for the planar ice samples, the charge density distribution in polar coordinates that gives rise to a nearly equipotential surface is given by Ciftja (2020) and McDonald (2002)

$$\sigma_{\mathrm{eq}}(r) = \begin{cases} \dfrac{Q}{2\pi R_b} \dfrac{1}{\sqrt{R_b^2 - r^2}}, & r \leqslant R_b \\ 0, & r > R_b. \end{cases} \tag{2}$$

At the origin, $\sigma_{\mathrm{eq}}(0) = \frac{1}{2}\frac{Q}{\pi R_b^2}$ and at the boundaries, $\lim_{|r|\to R_b} \sigma_{\mathrm{eq}}(r) = \infty$ for $Q > 0$. For the first two charge distributions, the potential is determined by integrating over the disk

$$V_q(r,z) = \frac{1}{2\epsilon_0} \int_0^{R_b} \frac{r\sigma(r)}{\sqrt{r^2 + z^2}} \mathrm{d}r. \tag{3}$$

These two charge distributions are plotted in Fig. 2a) with $Q = q_e$ where $q_e = 1.602 \times 10^{-19} C$ is the fundamental charge. The third case considered is a uniform surface charge distribution with screening charges present inside a film with finite thickness $t = 10$ nm and relative

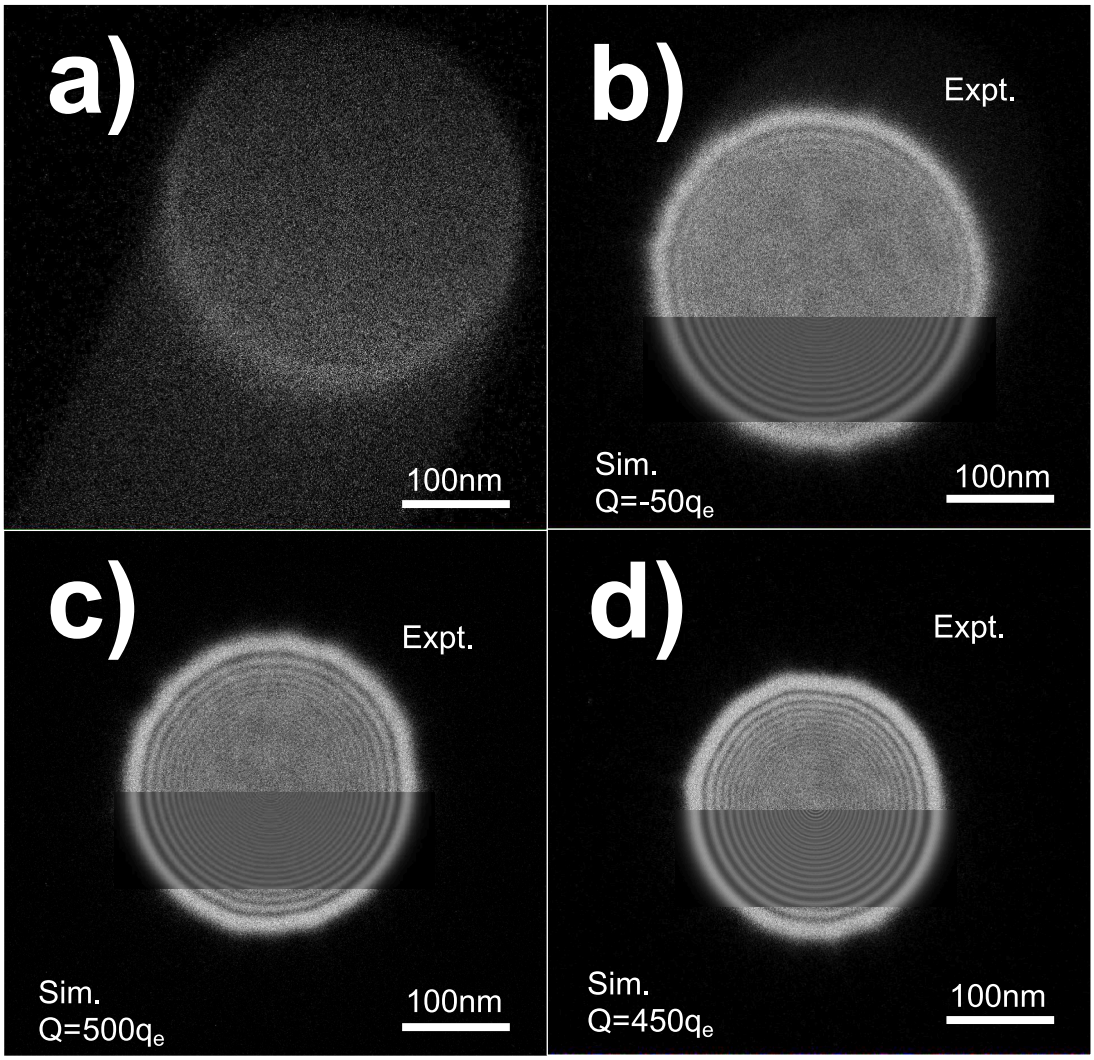

Fig. 1. Selected frames from a movie of the central defocused diffraction spot from a 913 nm diameter and 1.51$e^-/Å^2/s$ electron dose-rate beam centered on an ice film recorded at 40 fps. a) The first frame (0.04$e^-/Å^2$ accumulated dose), b) the second frame (0.08$e^-/Å^2$), c) the fifth frame (0.19$e^-/Å^2/s$), and d) the last frame (14.16$e^-/Å^2$). b)–d) show the fits to simulated data (superimposed strip at lower half) using the near equipotential surface charge distribution and the sample charge used for the simulation.

dielectric constant $\epsilon_r = 3.16$ for ice at liquid nitrogen temperatures (Petrenko, 1993). In this case, the potential at each point given by Malac et al. (2012)

$$dV_{sq}(r,z) = \frac{d\sigma(r)}{4\pi\epsilon_0\epsilon_r}\frac{zt}{(r^2+z^2)^{3/2}}. \quad (4)$$

This potential is integrated over a disk with uniform charge density.

The electrical potential distributions from these three charge distribution models are shown in Fig. 2d-f) where the vertical dotted lines represent the boundaries of the illuminated area. The uniform charge distribution with unscreened charges (Fig. 2d) has a non-uniform potential distribution on the illuminated sample surface. Both the equipotential charge distribution and screened uniform charge distributions have relatively uniform surface potentials in the illuminated areas. The equipotential charge distribution has 18 mV surface potential at the center and 10 mV at the edges of the illuminated area per q_e distributed charge.

The uniform charge distributions with and without screening charges were previously considered in Malac et al. (2012) for the case of a carbon film hole-free phase-plate. The equipotential charge distribution is newly considered here. For the phase-plates composed of conductive thin films, the assumption of a uniform charge distribution is reasonable. For the case of ice with a low charge mobility, a non-uniform charge distribution is likely to occur within the illuminated area. The infinite charge density at the edges of the illuminated area in the equipotential charge distribution model are of course not physical. However, by simulating the surface charge distribution based on a simple secondary electron emission model, a similar charge distribution is calculated as shown in Fig. 2c). In this model, the sample was assumed to have zero charge mobility. Each primary electron hitting an area of the sample releases a secondary electron; leaving behind a charge of $+q_e$. This secondary electron will then land onto an adjacent area of the sample and leave a fractional negative charge according to a Poisson distribution. If all secondary electrons return to the sample, the central portion of the illuminated area will be slightly negatively charged while the inner edges of the illuminated area are positively charged. If we allow for a certain percentage of secondary electrons to be lost to vacuum, as does happen or else SEM imaging would not be possible, the charge in the central region of the sample is positively charged. The areas just outside the illuminated areas become negatively charged. Thus, this simple secondary electron emission model suggests that a charge distribution close to the equilibrium charge distribution is possible and

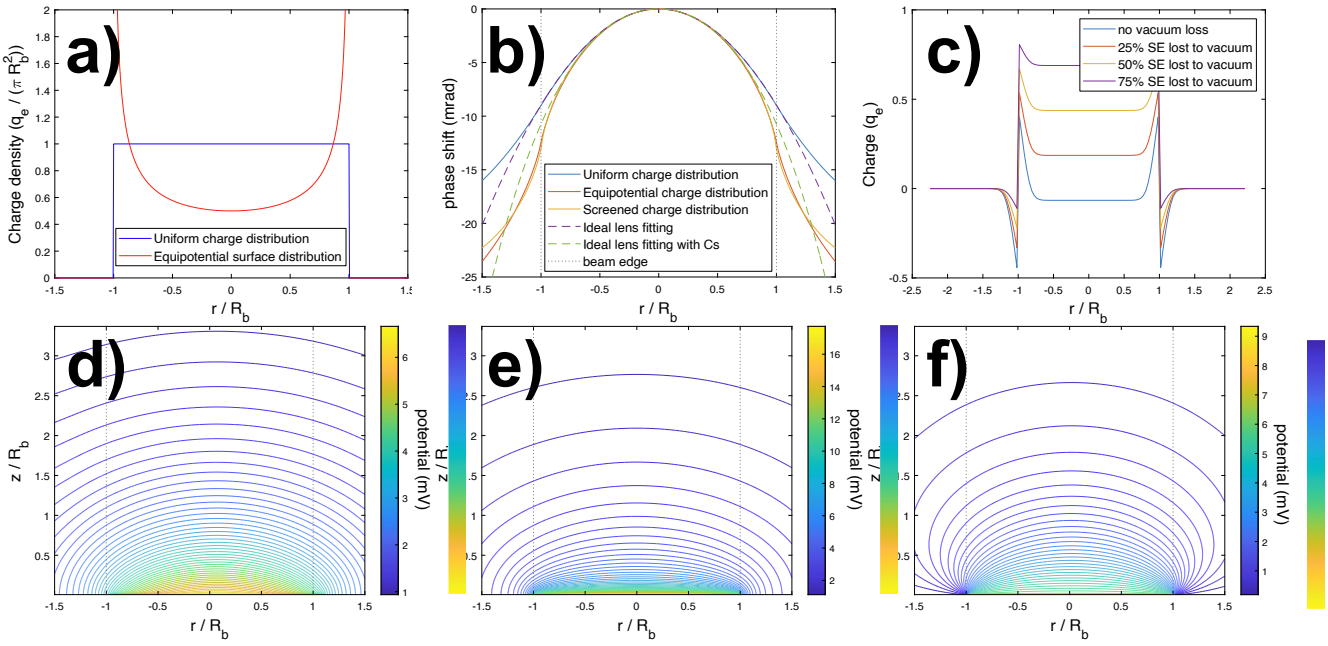

Fig. 2. Charge distribution models and their associated electrical potential distributions. a) Two charge distribution models of an equipotential surface and a uniform charge surface. The charge distributions are plotted for one $q_e = 1.602 \times 10^{-19}$ C charge in the illuminated area. b) Phase profiles calculated for electrons passing through the three charge distributions. Fits to ideal lenses and ideal lenses with third order spherical aberration are shown. The vertical dotted lines represent the boundaries of the illuminating electron beam. The uniform and equipotential charge distributions are calculated for one q_e charge. The screened charge distribution is calculated for 1350 q_e charge. c) Surface charge distribution model due to secondary electron emission. Plots for different percentages of secondary electrons effectively lost to vacuum are shown. d) Contour plot of potential distribution around a uniform surface charge distribution with one q_e charge. e) Contour plot of the potential distribution around a equipotential surface charge distribution with one q_e charge. f) Contour plot of the potential distribution around a screened uniform surface charge distribution with 1350 q_e charge.

reasonably applied to this situation. Note that the finite conductivity of the actual samples will also change the charge distribution from the secondary charge emission model as will changes in surface potentials from each accumulated charge. This simple model is merely used to demonstrate that higher charge densities at the edge of the illuminated area is possible in the limit of low electrical conductivity and is not intended to be a complete description of how charges build up on a sample.

The relative phase shift profiles on an electron plane wave passing through the three charge distribution models was calculated using

$$\varphi_E(r,\theta) = 2C_E \int_0^{+\infty} V(r,z)\mathrm{d}z \tag{5}$$

where C_E is the phase prefactor equal to 6.53rad $V^{-1}\mu m^{-1}$ at 300keV. The factor of two accounts for the potential being symmetric on either side of the film (assuming no other effect from the film material). The phase profiles calculated from the three charge distribution models are shown in Fig. 2b). For the unscreened uniform and equilibrium charge distributions, the phase-profile was calculated for $Q = q_e$ while the phase profile for the screened uniform charge distribution was calculated using $Q = 1350\ q_e$ to give a comparable phase shift magnitude. From this, it is immediately obvious that a screened charge requires a much larger total charge on the sample than unscreened charges. The charge on the screened charge distribution relative to unscreened charge distributions will depend on the material and geometrical parameters t and ϵ_r. The calculated phase profiles are compared to the ideal lens phase shift profile

$$\Delta\varphi_{\mathrm{ideal}} = -\frac{\pi r^2}{\lambda f} \tag{6}$$

where $\lambda = 1.97$ pm is the wavelength of 300 keV electrons and f is the lens focal length. Inside the illuminated area, the phase shift profile of the unscreened uniform charge distribution is shown to exactly follow an ideal lensing profile with a focal length of 37 m. The phase profiles of the equilibrium and screened charge distributions are nearly identical within the illuminated area. They can be seen to have slightly stronger phase shifts at the edges due to spherical aberrations. In their inner regions, the phase profiles also closely match the ideal lensing profile. The fit of these two profiles to an ideal lens plus third-order spherical aberration shows that there are still some higher-order spherical aberrations present at the edges of the illuminating areas.

2.3. Charge quantification with Fresnel patterns

To quantify the charging behavior, we simulated Fresnel propagation of the electron wave from an aperture with a slight misconjugation (defocus) of the condenser and object planes. The fit of the simulated Fresnel pattern and the beam image is shown in Fig. S2b). The phase profiles obtained from the charge distribution models were then applied at the object plane and further Fresnel-propagated to the detector plane. The fits between the experimental and simulated Fresnel fringing patterns are shown in Fig. S3 for the three charge distribution models. All three models could successfully fit the first few Fresnel fringes but could not fit the inner fringes well. The unscreened uniform charge distribution could not fit the variation in fringe amplitudes while the other two models did so successfully. Further, for the unscreened uniform charge distribution, a unique combination of sample charge and simulated propagation distance from sample plane to detection plane that best fit the experimental data could not be found. For the other two models, a unique set of parameters produced a best fit. The performance of the equipotential surface charge distribution and the screening charge distribution were nearly identical as their phase profiles are nearly identical within the illuminated area. However, the equipotential model does fit the amplitude distribution of the innermost fringes better. For the rest of this study, we quote results from the equipotential charge

distribution model as its underlying physics follows more closely the charge mobility limitations of this sample. The sample charges calculated are also more reasonable given the low electron dose-rate and low secondary electron emission coefficient at high accelerating voltages. While some degree of screening is probable in all types of samples, the effect of screening may not be as strong as predicted by Eq. 4.

Using this Fresnel propagation simulation, the experimentally measured Fresnel patterns in individual frames were fit by varying the total charge on a simulated sample Q and the object-detection plane separation distance z_p.

Example comparisons of the simulated and experimental patterns are shown in Fig. 1b)-d). The experimental Fresnel fringes could be fit with the simulated fringe patterns up to ± 50 q_e charge resolution and the propagation distance was sensitive to within ± 0.05 mm. While the fringe amplitudes and separations were affected by both the charge magnitude and propagation distance, the charge magnitude predominantly affected the amplitude distribution of the fringes while the propagation distance predominantly affected the fringe spacings.

3. Results and discussion

3.1. Ice film interactions with the electron beam

The diffraction spot beam radii were measured and plotted against the accumulated electron dose in Fig. 3a)-c). The beam radius plots in Fig. 3a) and b) are from various ice films suspended inside the quantifoil holes illuminated with the highest and lowest dose-rate conditions. All samples were observed to have an exponential decrease in beam radius when first illuminated until reaching a nearly steady-state radius. If a strong diffraction overfocus were used instead, the beam radius would increase up to a steady-state rather than decrease. For a few samples, the radius in the nearly steady-state region had a very slight linear increase with accumulated dose. Some slight fluctuations in beam radius beyond measurement noise is also observable. All beam radius curves could be closely fit to an exponential function with a linear term. It is expected that the image defocus applied for contrast transfer function (CTF) corrections would also follow such behaviors. Application of such a dose-dependent defocus to image pre-processing steps in single-particle workflows may improve the achievable resolution although finding the correct parameters for the function may be challenging. It was also observed that each fresh beam exposure resulted in an initial rapid beam radius change - ruling out any pre-exposure to reduce charging effects on data. Recently, there have been some reports that the use of pulsed electron sources leads to reduced sample damage (VandenBussche and Flannigan, 2019; Kisielowski et al., 2019; Choe et al., 2020). If the time between pulses is long enough, it may be possible that charge accumulation is reduced. The effect of stroboscopic sources on charging could be later investigated with the Fresnel diffraction technique.

The blue crosses in Fig. 3d) represent the accumulated dose at which the exponential decrease in beam radius transitions to a nearly steady-state radius value (as quantified by a $1/e^2$ threshold for the normalized beam radius curve; e being Euler's number). These values are averaged over all samples measured at a given dose-rate. Here, above a dose-rate threshold between 0.36 and 0.48$e^-/Å^2/s$, the dose accumulated before achieving the nearly steady-state condition is about

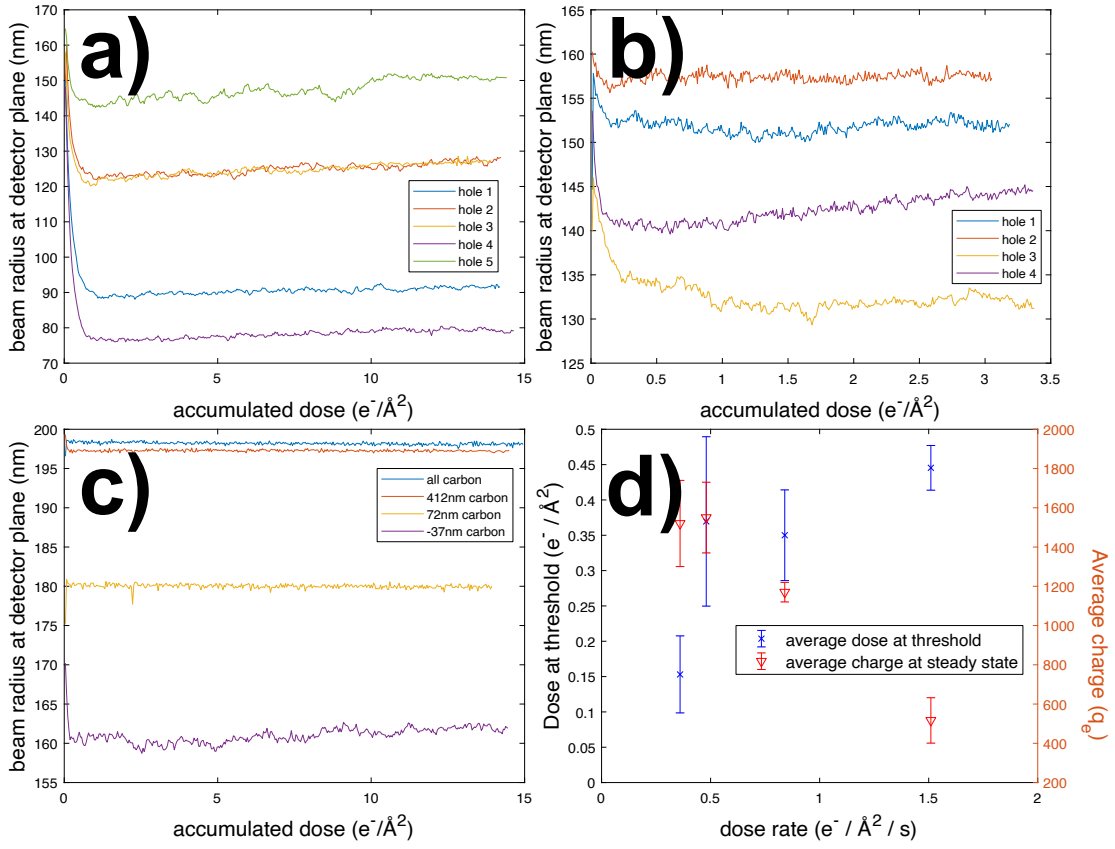

Fig. 3. a-c) Plots of the diffraction disc beam radius as a function of accumulated dose as measured from Fresnel diffraction movies recorded at 40 fps. a) Various ice films irradiated with 1.51$e^-/Å^2/s$, b) various ice films irradiated with 0.36$e^-/Å^2/s$, c) carbon film irradiated with 1.51$e^-/Å^2/s$ (blue line) and illuminated ice films with the surrounding carbon film moved into the illumination area by varying amounts. d) (left axis) The average electron dose at which the diffraction disc radius drops below a threshold value defined as $1/e^2$ of the normalized disc radius for various dose-rates. (right axis) The average charge on the samples as determined by the charge value which gave the best fit to frames in the semi-stable regions for various dose-rates. The error bars represent the standard deviation between 4 samples under the same dose-rate conditions.

$0.4e^{-}/Å^2$. Below this dose-rate threshold, the dose required to achieve the nearly steady-state condition is smaller. If it were not possible to correct for the defocus variations in the initial frames, this suggests that acquiring images at low dose-rates would be desirable as the steady-state region is achieved at a lower accumulated dose.

Frames in the nearly steady-state region of the sample were fit using the Fresnel pattern simulations to determine the equilibrium charge state of individual samples. The charge state among different sample holes under the same dose-rate conditions were averaged and plotted with red triangles in Fig. 3d). This shows a dependence of the equilibrium charge state of samples on the imaging dose-rate conditions. Higher dose-rates produce a smaller equilibrium charge state. However, up to a dose-rate threshold near $0.5e^{-}/Å^2/s$, the equilibrium charge state is constant. This is the opposite behavior to the dose-rate dependence of the average accumulated dose required to achieve temporal charge equilibrium (blue crosses Fig. 3d). Presumably, these dose-rate dependencies are related to the rate of SEs emitted by the sample at different conditions and with possible changes in charge mobility. It is unknown whether having a higher equilibrium sample charge state will damage particles faster. A higher charge state could indicate a higher radical concentration within samples and cause faster degradation. Higher charges would also induce stronger electric fields at the edges of the illuminated areas that could damage samples as previously explored by Jiang and Spence (Jiang, 2016). Previous studies on ice (Chen et al., 2008; Karuppasamy et al., 2011) and glass (Jiang and Spence, 2012) have indicated that lower dose-rates reduce beam-induced damage rates. However, the range of dose-rates used in the ice studies (1 to $> 10e^{-}/Å^2/s$) (Chen et al., 2008; Karuppasamy et al., 2011) is much larger than the dose-rate range used in the present study; only their lowest dose-rates overlapping within the range studied here. Therefore, within "low dose-rate" imaging conditions, there may be an optimal condition that is not the lowest possible dose-rate afforded by microscope stability to achieve minimal sample damage per incident electron.

The charge state from individual frames of a dataset were measured as shown by the blue circles in Fig. 4a). The measured values in the first frames as well as several later frames are shown. It is observed that the first exposure of the sample to the electron beam results in a very rapid increase of the charge state as is expected from the beam radius variation. The charge fitting reveals that samples can initially possess a small negative charge before accumulating positive charges. This can be because of the accumulation of secondary electrons released from nearby exposed areas as was previously reported by Russo and Henderson (2018) and utilized for paraxial charge compensation by Berriman and Rosenthal (2012); Vinothkumar et al., 2016. After a few frames, the charge state rapidly fluctuates before becoming more consistent in the semi-stable region. Inside the beam, contrast fluctuations like the "bee-swarm" effect (Dove, 1964; Russo and Henderson, 2018) ascribed to microscopic charge fluctuations are visible (supp. dat. 1). While these contrast fluctuations are semi-random, on ice, they can be observed to have an overall radial in-out motion that correspond to the small beam-radius fluctuations in the semi-stable region of Fig. 3a) and b). These charge fluctuations may be due to the charge carrier mismatch at the interface of the protonic ice and electronic carbon (Petrenko, 1993) which prevents a stable direct current flow. The charge carrier mismatch leads to a "frozen-in" potential difference at the interface (reported to be about 1.5 V for -10 °C ice (Petrenko, 1993)) which must be overcome for charge to flow. Based on the surface potential calculated in Fig. 2e) for 1 q_e and the equilibrium charge states in Fig. 3d), all the samples reach potential between 7-30 V at the center of the illuminated area and 4-17 V at the edges, depending on the applied dose-rate. As the ice used in this study was frozen much more rapidly, maintained at a much colder temperature, and contains other species besides water, the "frozen-in" potential may be larger here than that reported by Petrenko (1993). Based on the equilibrium charge distribution model and the measured charge states, the radial electric field component at the edge of the illuminated area was calculated to be between 2.0-8.4 $\times$ 10^6 V cm^{-1} depending on the applied dose-rate. The strength of the field rapidly drops off towards the center of the beam (1.9-8.0 $\times$ 10^4e V cm^{-1} at half the beam radius). The field required to cause the dielectric breakdown of ice has previously been measured (Kohno et al., 1980) as about 0.5 $\times$ 10^6e V cm^{-1} with the addition of silica beads roughly doubling the necessary field strength. Taking into account the slight discrepancies actual charge distributions will have with the equipotential charge distribution model used and the effect of buffer and embedded proteins within the ice, it is likely that the dielectric breakdown is achieved at the edge of the illuminated area; allowing charge to flow out briefly before accumulating again. It may be possible to improve the electrical contact between ice and carbon by plunging a grid while under bias (near the equilibrium potential) as previously performed for other ice-metal interfaces (Evtushenko and Petrenko, 1988; Petrenko, 1993; Hobbs, 1974). To do so without affecting the embedded proteins may prove challenging.

Not only does the charge state of the ice films rapidly fluctuate upon initial exposure to the electron beam but the sample height does as well; as shown by the red stars in Fig. 4a) (scale on right ordinate). It should be noted that these distances are not calibrated to the vertical sample position; though they are related. As the sample is part of a continuous film that continues outside the illuminated area, it is likely that the ice film is doming to produce the observed sample height changes. The reduction of visibility of the inner Fresnel fringes in the first few frames (Fig. 1) may also indicate strong vertical sample movement. However,

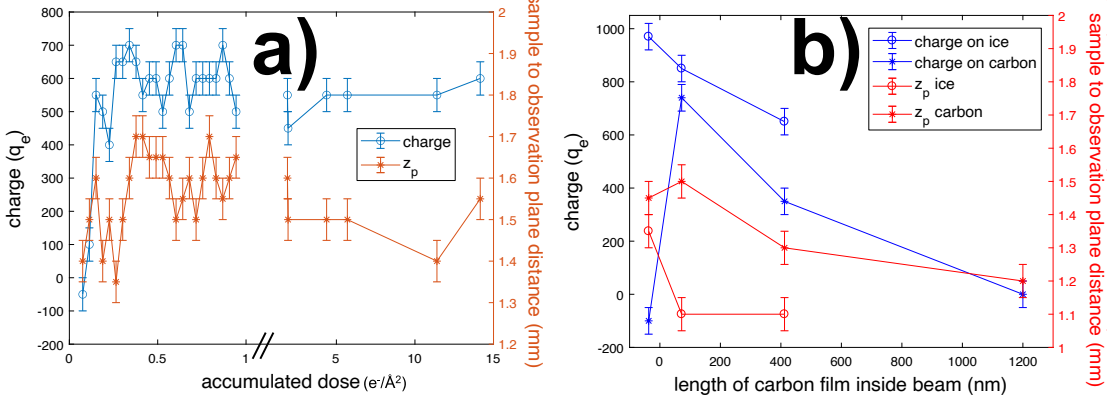

Fig. 4. a) Fitted charge Q (left y-axis) and propagation distance z_p (right y-axis) values for an ice film sample exposed to a $1.51e^{-}/Å^2/s$ dose-rate. The double-slash on the x-axis represents a jump in the accumulated dose scale markings in order to make the behavior at low accumulated dose more visible. b) Fitted charge and propagation distance values for an ice film sample with the surrounding carbon film entering inside the beam area imaged with a $0.48e^{-}/Å^2/s$ dose-rate.

this degradation of the inner fringes is likely due to the radial motion of the whole beam that shifts all fringes and affects the visibility of the finer inner fringes more.

That ice films under electron beam illumination vibrate like a drumskin was previously proposed by Brilot et al. (2012). In their model, beam-induced vibrational motion causes translations and rotations of the embedded particles as well as plastic deformation of the film. The current work demonstrates that both film movement (contributing to beam-induced sample motion) and charge state variations occur upon electron beam exposure. Both effects affect the image defocus through physical sample height and lensing strength changes.

The charge distribution model used in the present study assumes a completely flat film of negligible thickness. It may be possible to improve the match between experimental and simulated Fresnel diffraction patterns by including geometrical parameters such as film curvature to the model. This would allow for the doming behavior pointed out in this and previous studies as well as curvatures in the ice films that can be present from preparation before electron exposure (Noble et al., 2018). The addition of film curvature may improve the ability to fit inner Fresnel fringes more accurately although this necessitates more fitting parameters. As a more complete model is developed, data from more modern direct electron detectors with improved sensitivity and temporal resolution may allow for further insights into the dynamics of thin films upon electron beam exposure.

3.2. *Electron beam interactions at the ice-carbon interface*

When a carbon film was illuminated, no change in the beam radius with accumulated dose was observed and no charge was measured on the film Fig. S4, supp. dat. 2, and blue curve of Fig. 3c). Thus, in the cryogenic state, quantifoil carbon films have enough conductivity to not accumulate charges while illuminated with low dose-rates. Due to the higher contrast of the carbon film relative to ice, it is more difficult to discern the "bee-swarm" effect inside the diffraction disks although it is present. No overall radial motion is discernible.

When ice films were illuminated with some carbon inside the illuminated area, change in the beam radius was not observed except for when the carbon film was just outside the illuminated area as shown in Fig. 3c). It thus initially appears that the presence of a carbon film inside the illuminated area prevents charging. However, when a beam illuminating ice approaches the edge of a carbon film, the edges of the beam are distorted as shown in Fig. 5a). When a bit of carbon film is introduced inside the illuminated area, the beam can be observed to have two radii; from the ice region and carbon region as represented by the blue and red dotted circles in Fig. 5b). Thus, although illuminated areas containing some carbon did not appear to change beam radius with accumulated dose (Fig. 3c), a spatial charge gradient is present between the carbon and ice regions. The charge states in the ice and carbon films were fit separately for different amounts of carbon film in the illuminated area as shown by the simulation inserts in Fig. 5. The results are summarized in Fig. 4b) where the blue circles represent the charge state on ice and the blue star represents the charge state on carbon. The red circles and stars represent the simulation propagation distances on the ice and carbon. It is observed that despite the beam size staying stable with accumulated dose, the charge state of the ice film is non-zero. As less and less carbon is contained inside the illuminated area, the charge state on the ice is increased. However, the equilibrium charge state achieved with adjacent carbon film is lower than when only ice is illuminated with an equivalent dose-rate. The stability of the beam radius is likely due to the secondary electron emission rate from the carbon being higher than the ice – causing an almost immediate equilibrium charge state to be formed. Less illuminated carbon providing less neutralizing SEs would also account for the increased charge on the carbon film. When illuminated along-side an ice film, the carbon film also has a non-zero charge state. It could be that when the carbon is not grounded from all sides, it cannot completely purge its charge state; although it remains in equilibrium. When the carbon film is just outside of the illuminated area, it still has a small effect on the electron beam likely due to a difference in potential. More interestingly, the Fresnel fringing from the carbon influence suggests that it accumulates a slightly negative charge. This may be a manifestation of the accumulated negative charge at the edge of an illuminated area due to the secondary electron emission as predicted by Fig. 3c). The z positions of the ice and carbon films are furthest when only a bit of carbon is in the illuminated area. As the "doming" of the ice film would mechanically be assumed to be highest at the center of the ice film, the z position difference may just be due to the induced curvature of the ice film (as the fittings were performed on opposite ends of the beam).

The analysis in the current work demonstrates that insulating samples illuminated by an electron beam have a spatial charge distribution close to that of the equipotential charge distribution model. As the models do not take into consideration sample thickness, the distribution

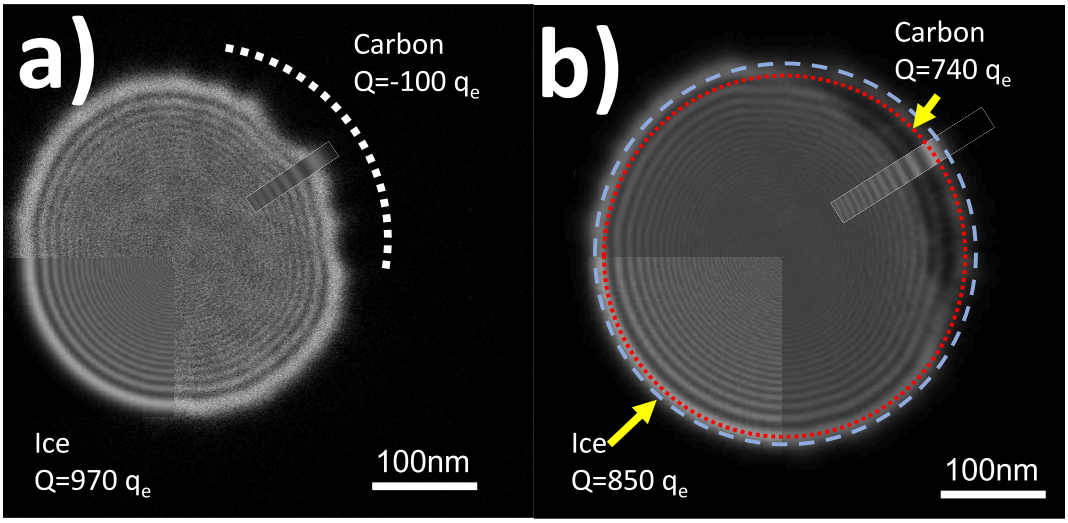

Fig. 5. a) Frame of the central diffraction disc when the electron beam is 72 nm away from the edge of the carbon film (represented by the dotted curve). b) Sum of frames of the central diffraction disc when a carbon film is 32 nm inside the area illuminated by the electron beam. The darker area is the carbon film. Red dotted and blue dashed circles show the radius associated with carbon and ice areas. Simulated Fresnel patterns for the carbon and ice areas and their associated charge values are also shown. (For interpretation of the references to colour in this figure legend, the reader is referred to the web version of this article.)

is in essence a projected charge. Therefore we do not explicitly determine the mechanism behind how the charge distribution comes to be. We hypothesize that the surface effect of secondary electron emissions are predominantly responsible for the achieved projected charge distribution. There have been suggestions that radiolysis products formed in ice during electron irradiation may increase the bulk conductivity of the illuminated region. No experimental measurements have been performed to test such a hypothesis. However, the fact that illumination of adjacent carbon films as shown here (and distant carbon films as used in paraxial charge compensation schemes) largely eliminates the temporal charging dynamics suggest that surface charge redistributions play a more dominant role than bulk (and thickness-dependent) effects – particularly within the first $e^-/Å^2$ of exposure. Further experiments are underway to test this. However, this is not to say that thickness of ice and carbon films play no role in their charging behaviors. Dedicated studies to investigate the role of sample thickness on charging effects should be performed.

With the Fresnel diffraction experiments and modeling, some dose-rate dependent behavior of illuminated insulating films have been revealed. In these experiments, Fresnel diffraction patterns were recorded and the fringe patterns fit to charge distribution models. Similar experiments can be performed with image data and have been reported before (Malac et al., 2012). In general, quantification of sample charges can be performed either by fitting to Fresnel diffraction data or fitting Thon rings in Fourier transforms of image data (Malac et al., 2017). The accuracy of these techniques is limited by the charge distribution models used. For beam-sensitive samples, the diffraction-based technique allows for higher signal acquisitions with higher fringe contrasts using the same accumulated dose as nearly all the scattered electrons are captured within the finite size of the camera. This allows for a fine temporal/dose sampling of the charging dynamics in the present work. This technique could be used to further characterize the effects of different support grids such as gold foils (Russo and Passmore, 2014), graphene membranes (Sader et al., 2013), and different buffer conditions on charging dynamics.

Based on the results of this study, several suggestions and comments can be made about cryo-EM data collection and analysis. When a sample is exposed to an electron beam, a rapid evolution of the charge state occurs. This causes both accumulation of positive charges within the sample and deformation of the ice film which affect the optical imaging parameters. This change is most prominent in the first 0.5 $e^-/Å^2$ of exposure. However, the lensing effects can still evolve with further electron exposure. To best correct for the CTF, constant parameters over the exposure time cannot be used. That the usual practice of including some of conductive support grid in the illumination area is beneficial for the charge stability of the sample was confirmed. However, it should be noted that the optical parameters near the conductive film interface can be quite different from areas far from the interface. Thus, within a micrograph, spatially dependent optical corrections should be applied. The most accurate charge distribution model among those considered was the equipotential model Eq. (2) which has a non-uniform charge distribution. The edges of the illuminated areas thus have the highest charge densities and strongest electric fields. Jiang (2016) has demonstrated that samples in strong electric fields can be damaged more rapidly. This suggests that particles near the edges of illuminated areas and near the support film edge may be damaged more rapidly than those far from such interfaces. Finally, the effect of electron dose-rate in low-dose regimes should be more carefully considered and studied – especially if the effects of the dose-dependent optical parameters are not corrected. Using a dose-rate below $0.4e^-/Å^2/s$ will allow for more movie frames to contribute to the final reconstruction if no dose-dependent defocus corrections are applied. However this will cause more charge to be accumulated on the sample over time and may damage particles faster.

4. Conclusions

This study investigated the temporal and spatial charge distributions on free-standing amorphous ice films upon exposure to a parallel and dose-rate controlled electron beam. Our data reveal that upon irradiation, the film undergoes a rapid charge buildup until a near-equilibrium state with grounding currents and secondary electron recapture is achieved. The total dose to achieve equilibrium and how much charge is then accumulated both depend on the dose-rate. The charge buildup causes the film itself to behave as a weak electrostatic lens which changes the optical imaging parameters dynamically. As the film charges, it also vibrates physically, thereby changing the object-lens separation. Both the lensing effect and the vibrations affect the contrast transfer function of early frames in dose-fractionated movies relative to later frames. The introduction of a carbon film into the illuminated area greatly reduces the temporal charging dynamics. However, non-zero charge builds up on both the ice and carbon films within the illuminated area – creating a charge gradient. Therefore, near the edge of a carbon film, a gradient of imaging parameters exists.

By taking into account such beam-induced effects, image processing techniques may be refined to extract more information from dose-fractionated image stacks. Sample preparation techniques may also be designed such as to improve the electrical contact at ice-carbon interfaces. With the time-resolved Fresnel diffraction technique described here, the effect of different buffers and support grids on the charging process can be further studied as well as charging processes in other beam-sensitive samples.

Author contributions

M.T.S. conducted the experiments, wrote data analysis scripts, developed the charging models, analyzed the data, and wrote the manuscript. A.M. performed initial microscopy and K2 data collection setup. S.S prepared samples. M.T.S, A.M. and M.W. conceptually designed the experiments. M.B. provided the framework for modeling and simulation. M.W. supervised the project. All authors discussed the results and edited the paper.

Declaration of Competing Interest

The authors declare the following financial interests/personal relationships which may be considered as potential competing interests: Matthias Wolf reports financial support was provided by Japan Agency for Medical Research and Development. Makoto T Schreiber reports financial support was provided by Japan Society for the Promotion of Science.

Acknowledgments

M.T.S. was supported by JSPS fellowship (DC1) 201820215, JSPS Kakenhi grant 18J20215 and Kakenhi Grant-in-aid for JSPS fellows 18J20132. M.W. was supported by the Platform Project for Supporting Drug Discovery and Life Science Research (BINDS) from AMED under Grant No. JP18am0101076. The OIST imaging section is acknowledged for use of the Cryo-EM facility. M.T.S and M.W. are grateful for direct funding from OIST.

Appendix A. Supplementary data

Supplementary data associated with this article can be found, in the online version, at https://doi.org/10.1016/j.yjsbx.2022.100081.

References

Berriman, J.A., Rosenthal, P.B., 2012. Paraxial charge compensator for electron cryomicroscopy. Ultramicroscopy 116, 106–114.

Brilot, A.F., Chen, J.Z., Cheng, A., Pan, J., Harrison, S.C., Potter, C.S., Carragher, B., Henderson, R., Grigorieff, N., 2012. Beam-induced motion of vitrified specimen on holey carbon film. J. Struct. Biol. 177 (3), 630–637.
Brink, J., Sherman, M.B., Berriman, J., Chiu, W., 1998. Evaluation of charging on macromolecules in electron cryomicroscopy. Ultramicroscopy 72 (1), 41–52.
Brink, J., Gross, H., Tittmann, P., Sherman, M., Chiu, W., 1998. Reduction of charging in protein electron cryomicroscopy. J. Microsc. 191, 67–73.
Cazaux, J., 1993. Some physical descriptions of the charging effects in insulators under irradiation. Springer.
Cazaux, J., 1995. Correlations between ionization radiation damage and charging effects in transmission electron microscopy. Ultramicroscopy 60 (3), 411–425.
Cazaux, J., 2004. Charging in scanning electron microscopy "from inside and outside". Scanning 26 (4), 181–203.
Cazaux, J., 2006. e-induced secondary electron emission yield of insulators and charging effects. Nucl. Instrum. Methods Phys. Res. Sect. B 244 (2), 307–322.
Chen, J.Z., Sachse, C., Xu, C., Mielke, T., Spahn, C.M., Grigorieff, N., 2008. A dose-rate effect in single-particle electron microscopy. J. Struct. Biol. 161 (1), 92–100.
Choe, H., Ponomarev, I., Montgomery, E., Lau, J.W., Zhu, Y., Zhao, Y., Liu, A., Kanareykin, A., Jing, C., 2020. Mitigation of radiation damage in macromolecules via tunable ultrafast stroboscopic TEM. bioRxiv.
Ciftja, O., 2020. Results for charged disks with different forms of surface charge density. Results Phys. 16, 102962.
Curtis, G., Ferrier, R., 1969. The electric charging of electron-microscope specimens. J. Phys. D: Appl. Phys. 2 (7), 1035.
Dove, D., 1964. Image contrasts in thin carbon films observed by shadow electron microscopy. J. Appl. Phys. 35 (5), 1652–1653.
Evtushenko, M.M.A.A., Petrenko, V., 1988. Experimental study of electrical properties of ice grown in constant electric field. Soviet Phys.- Solid State 30, 2133–2138.
Grant, T., Grigorieff, N., 2015. Measuring the optimal exposure for single particle cryo-EM using a 2.6 Å reconstruction of rotavirus VP6. eLife 4.
Hobbs, P.V., 1974. Ice physics. Oxford.
Jiang, N., 2016. Beam damage by the induced electric field in transmission electron microscopy. Micron 83, 79–92.
Jiang, N., Spence, J.C., 2012. On the dose-rate threshold of beam damage in TEM. Ultramicroscopy 113, 77–82.
Karuppasamy, M., Karimi Nejadasl, F., Vulovic, M., Koster, A.J., Ravelli, R.B., 2011. Radiation damage in single-particle cryo-electron microscopy: effects of dose and dose rate. J. Synchrotron Rad. 18 (3), 398–412.
Kisielowski, C., Specht, P., Freitag, B., Kieft, E.R., Verhoeven, W., van Rens, J.F., Mutsaers, P., Luiten, J., Rozeveld, S., Kang, J., et al., 2019. Discovering hidden material properties of MgCl2 at atomic resolution with structured temporal electron illumination of picosecond time resolution. Adv. Funct. Mater. 29 (11), 1807818.
Kohno, T., Nakazawa, H., Kosaki, M., Horii, K., 1980. Electrical breakdown of ice at cryogenic temperatures. IEEE Trans. Electr. Insul. 1, 27–32.
Malac, M., Beleggia, M., Kawasaki, M., Li, P., Egerton, R.F., 2012. Convenient contrast enhancement by a hole-free phase plate. Ultramicroscopy 118, 77–89.
Malac, M., Hettler, S., Hayashida, M., Kawasaki, M., Konyuba, Y., Okura, Y., Iijima, H., Ishikawa, I., Beleggia, M., 2017. Computer simulations analysis for determining the polarity of charge generated by high energy electron irradiation of a thin film. Micron 100, 10–22.
McDonald, K.T., 2002. Conducting ellipsoid and circular disk. Princeton Univ., Princeton, NJ.[Online]. Available:http://puhep1.princeton.edu/mcdonald/examples/ellipsoid.pdf.
Noble, A.J., Dandey, V.P., Wei, H., Brasch, J., Chase, J., Acharya, P., Tan, Y.Z., Zhang, Z., Kim, L.Y., Scapin, G., et al., 2018. Routine single particle cryoEM sample and grid characterization by tomography. eLife 7, e34257.
Petrenko, V.F., 1993. Electrical properties of ice (Technical report). Regions Research and Engineering Lab, Cold Hanover NH.
Renoud, R., Attard, C., Ganachaud, J., Bartholome, S., Dubus, A., 1998. Influence on the secondary electron yield of the space charge induced in an insulating target by an electron beam. J. Phys.: Condens. Matter 10 (26), 5821.
Rubinstein, J.L., Brubaker, M.A., 2015. Alignment of cryo-EM movies of individual particles by optimization of image translations. J. Struct. Biol. 192 (2), 188–195.
Russo, C.J., Henderson, R., 2018. Charge accumulation in electron cryomicroscopy. Ultramicroscopy 187, 43–49.
Russo, C.J., Henderson, R., 2018. Microscopic charge fluctuations cause minimal contrast loss in cryoEM. Ultramicroscopy 187, 56–63.
Russo, C.J., Passmore, L.A., 2014. Ultrastable gold substrates for electron cryomicroscopy. Science 346 (6215), 1377–1380.
Sader, K., Stopps, M., Calder, L.J., Rosenthal, P.B., 2013. Cryomicroscopy of radiation sensitive specimens on unmodified graphene sheets: reduction of electron-optical effects of charging. J. Struct. Biol. 183 (3), 531–536.
Scheres, S.H., 2014. Beam-induced motion correction for sub-megadalton cryo-EM particles. eLife 3.
VandenBussche, E.J., Flannigan, D.J., 2019. Reducing radiation damage in soft matter with femtosecond-timed single-electron packets. Nano Lett. 19 (9), 6687–6694.
Vinothkumar, K.R., Henderson, R., 2016. Single particle electron cryomicroscopy: trends, issues and future perspective. Q. Rev. Biophys. 49.
Zheng, S.Q., Palovcak, E., Armache, J.-P., Verba, K.A., Cheng, Y., Agard, D.A., 2017. MotionCor2: anisotropic correction of beam-induced motion for improved cryo-electron microscopy. Nat. Methods 14 (4), 331.
Zivanov, J., Nakane, T., Scheres, S.H., 2019. A Bayesian approach to beam-induced motion correction in cryo-EM single-particle analysis. IUCrJ 6 (1).